American Mineralogist, Volume 109, pages 729–737, 2024

Pressure-induced phase transitions in Ni-bearing ferrosilite (Ni-$En_{31}Fs_{65}$)

Jingui Xu[1,2,*], Dawei Fan[1,*,‡], Dongzhou Zhang[2,†], Bo Li[3], Wenge Zhou[1], and Przemyslaw Dera[2]

[1]Key Laboratory for High-Temperature and High-Pressure Study of the Earth's Interior, Institute of Geochemistry, Chinese Academy of Sciences, Guiyang, Guizhou 550081, China
[2]Hawai'i Institute of Geophysics and Planetology, School of Ocean and Earth Science and Technology, University of Hawai'i at Manoa, Honolulu, Hawaii 96822, U.S.A.
[3]Research Institute of Petroleum Exploration & Development-Northwest (NWGI), PetroChina, Lanzhou 730060, Gansu, China

Abstract

Orthopyroxene is an abundant mineral in subducting slabs. Studying its phase transitions at high pressure is important to the understanding of mineralogy of subducting slabs in the deep Earth. Synchrotron-based single-crystal X-ray diffraction experiments were conducted on a synthetic Ni-bearing ferrosilite (Ni-$En_{31}Fs_{65}$) at pressures up to 33.8 GPa. Three phase transitions were observed at 12.1(6), 15.6(6), and 31.3(25) GPa. The first two phase transitions in Ni-$En_{31}Fs_{65}$ resemble the previously described phase transitions in Ni-free Fe-rich orthopyroxenes, i.e., the initial α-opx (*Pbca*) transforms to β-opx ($P2_1/c$), then the latter transforms to γ-opx (*Pbca*). This indicates that the incorporation of a few mol% $NiSiO_3$ does not influence the phase transition path of Fe-rich orthopyroxene. After the third phase transition, the structure ($P2_1ca$) of Ni-$En_{31}Fs_{65}$ resembles the previously reported β-popx observed in En_{90} at high pressure, although the onset pressure of the phase transition in Ni-$En_{31}Fs_{65}$ is ~7 GPa lower than that in En_{90}. β-popx has a post-pyroxene structure that contains fivefold- and sixfold-coordinated Si cations. Our results indicate that the post-pyroxene structure is β-popx ($P2_1ca$) for either Fe-poor or Fe-rich orthopyroxenes, although the phase transition path before the pyroxene → post-pyroxene is compositionally dependent. Additionally, unlike the second and third transitions, whose onset pressures are monotonously decreased by increasing Fe content, the Fe effect on shifting the first transition is much more significant for orthopyroxenes within En <50 mol% than that within En >50 mol%.

Keywords: Pyroxene, phase transition, single-crystal X-ray diffraction, high pressure

Introduction

Orthopyroxene is a major rock-forming mineral in the subducting oceanic slabs. A typical subducting slab is composed of three layers, with the basaltic crust layer atop, and the residual harzburgite and lherzolite at the middle and bottom, respectively (Ringwood 1982). Harzburgite and lherzolite commonly contain more than 20 vol% orthopyroxene (Bodinier and Godard 2007). It has been proposed that pyroxene minerals could survive as metastable phases in cold subducting slabs as the low-temperature conditions largely inhibit the pyroxene-majorite transition (Nishi et al. 2013; van Mierlo et al. 2013). Therefore, investigating the phase transitions of orthopyroxene at high pressures and high temperatures is important to the understanding of the mineralogy of subducting slabs.

In recent years, room-temperature high-pressure single-crystal X-ray diffraction (SCXRD) has revealed several high-pressure phases of orthopyroxene. The initial orthopyroxene (α-opx, *Pbca* space group) transforms into a monoclinic structure (β-opx, $P2_1/c$) at pressures ranging from 6 to 16 GPa depending on the contents of Fe, Al, and Ca (e.g., Lin et al. 2005; Dera et al. 2013a; Zhang et al. 2012, 2013a, 2013b; Finkelstein et al. 2015; Xu et al. 2020; Li et al. 2022). With increasing pressure, β-opx transforms into α-popx ($P2_1ca$; Finkelstein et al. (2015) when the molar percentage (M; mol%) of enstatite (En, $MgSiO_3$) of the sample is higher than ~80 mol%, otherwise it transforms into γ-opx (*Pbca*; Dera et al. 2013a). The onset pressure (12–31 GPa) of the β-opx → γ-opx transition is also dependent on the contents of Fe, Al, and Ca (Xu et al. 2020; Xu et al. 2022). After the β-opx → γ-opx transition, no further phase transitions have been observed; in comparison, the α-popx → β-popx ($P2_1ca$, post-pyroxene structure; Finkelstein et al. 2015) transition in $En_{90}Fs_{10}$ (Fs is ferrosilite, $FeSiO_3$) has been observed at ~40 GPa. It should be noted that the high-pressure SCXRD measurement (Xu et al. 2018) up to 34 GPa did not observe phase transition in end-member enstatite (En_{100}) after the α-opx → β-opx transition but high-pressure Raman spectroscopy experiment (Serghiou et al. 2000) revealed a new phase (at ~40 GPa) whose structure resembles that of the β-popx after the α-opx → β-opx transition. High-pressure and high-temperature SCXRD and Raman spectroscopy studies revealed that the α-opx → β-opx → γ-opx transitions could occur for orthopyroxenes under the pressure-temperature conditions of the cold slab center within the transition zone (Zhang et al. 2014; Xu et al. 2022).

Nonetheless, the compositional effects on the high-pressure phase transitions of orthopyroxene have not yet been well con-

* Co-corresponding authors E-mail: jgxu107@gmail.com, fandawei@vip.gyig.ac.cn
† Orcid 0000-0002-6679-892X
‡ Orcid 0000-0001-7840-2075

strained. On the one hand, β-popx is observed as the high-pressure phase for En_{90} after the β-opx → α-popx transition (Finkelstein et al. 2015). But it is still unclear whether β-popx is also the high-pressure phase of orthopyroxenes that are more Fe-rich than En_{90} after the β-opx → γ-Opx transition. On the other hand, Xu et al. (2022) found that, for the En-Fs solid solutions, varying Fe content has little effect on the pressure of the α-opx → β-opx ($P_{α-β}$) within M_{En} = 44–100, and suggested that the effect of varying Fe on $P_{α-β}$ is more significant within M_{En} = 0–44, which needs to be verified. Thus, studies on the high-pressure phase transitions of Fe-rich orthopyroxenes are needed to clarify these inconsistencies.

Other than Fe, Al, and Ca, Ni commonly occurs in natural orthopyroxene, and the NiO content in orthopyroxene can be as high as ~1 wt% in Ni-enriched mantle peridotite (Ishimaru and Arai 2008). Thus, experimental studies on Ni-bearing orthopyroxene could provide a more comprehensive understanding of the phase transitions of orthopyroxene group. Our recent study has reported that Ni-bearing enstatite ($Mg_{0.95}Ni_{0.05}SiO_3$) transforms from the initial α-opx into the β-opx at 13.5 GPa, but with increasing pressure, the β-opx does not transform into the γ-opx or the α-popx; instead, it transforms into a new high-pressure phase (β-opxII, $P2_1/c$ space group) at 29.8 GPa (Xu et al. 2018), indicating that the incorporation of a few mol% $NiSiO_3$ could change the phase transitions of orthopyroxene at high pressures. However, it remains unknown whether the incorporation of a few mol% $NiSiO_3$ would influence the phase transitions of Fe-rich orthopyroxenes at high pressures. Answering this question is important for modeling the metastable phases of Ni-, Fe-bearing orthopyroxene in the deep earth, which demands further studies on the high-pressure phase transitions of Ni-, Fe-bearing orthopyroxene.

Therefore, in this study, we performed high-pressure SCXRD experiments on a synthetic Ni-bearing ferrosilite to constrain the compositional (Ni and Fe) effects on the phase transitions of orthopyroxene.

Experiments

We synthesized the Ni-bearing ferrosilite from a mixture of high-purity SiO_2, MgO, Fe_2O_3, Fe, and NiO using a multi-anvil press apparatus at the Institute of Geochemistry, Chinese Academy of Sciences. The sample synthesis was conducted at 1000 °C and 3 GPa for 24 h, and the detailed description can be seen in the authors' previous study (Xu et al. 2018). The obtained crystals from the quenched samples were between 40–100 μm in size. Electron microprobe analyses (EMPA) were carried out using a JXA 8230, operating at an acceleration voltage of 15 kV and a beam current of 20 nA, and the focused beam was ~5 μm. The chemical formula was estimated as $Mg_{0.31}Fe_{0.65}Ni_{0.04}SiO_3$ (Ni-$En_{31}Fs_{65}$, hereafter).

We selected a crystal with a size ca. 40 × 20 × 10 $μm^3$ and loaded it into a short-symmetric diamond-anvil cell (DAC) for the ambient and high-pressure SCXRD experiments. The DAC was equipped with two type-I diamonds with 300 μm culet size and two Boehler-Almax-type WC seats, allowing a ±32 ° opening angle. A rhenium plate with an initial thickness of 250 μm was indented to ~50 μm to serve as the gasket, and a laser-drilled hole with 180 μm in diameter in the indented area was the sample chamber. The selected crystal, a small ruby sphere, and a gold foil were loaded into the sample chamber (Fig. 1) before loading neon as the pressure medium using the gas loading system at GSECARS, Advanced Photon Source (APS) (Rivers et al. 2008). The gold foil (Fei et al. 2007) was used as the pressure marker in the processes of high-pressure experiments.

The SCXRD experiments were carried out with a six-circle diffractometer at the experimental station 13-BM-C of APS, Argonne National Laboratory. The incident X-ray was monochromated to a wavelength of 0.434 Å with a focused beam size of 12 × 18 $μm^2$. A MAR165 CCD was used to acquire the diffraction image, and the tilting and rotation of the detector and the sample-to-detector distance were calibrated using LaB_6 powder as the diffraction standard (Zhang et al. 2017). We collected diffraction data at 27 different pressures from room pressure to 33.8 GPa. We noted that the sample chamber shrank with increasing pressure. As shown in Figure 1d the Re peaks occurred in the data collected at 33.8 GPa, indicating that high-quality SCXRD data cannot be ensured at higher pressures. At each pressure, the φ-rotation scan was with a step size of 1° and an exposure time of 1 s/°, and the rotation range was the same as the DAC opening angle. Besides, we collected increased diffraction peaks with multiple detector positions (Xu et al. 2017a) at 10 of the 27 pressures for full structure determination.

The diffraction images were processed using the GSE_ADA/RSV software package (Dera et al. 2013b) to extract the unit-cell information and peak intensities. The refined unit-cell parameters are shown in Online Materials[1] Table S1. We used SHELXL (Sheldrick 2008) software via Olex2 (Dolomanov et al. 2009) user interface to refine the crystal structure at different pressures, and the VESTA software (Momma and Izumi 2011) was used to calculate polyhedral parameters. We used

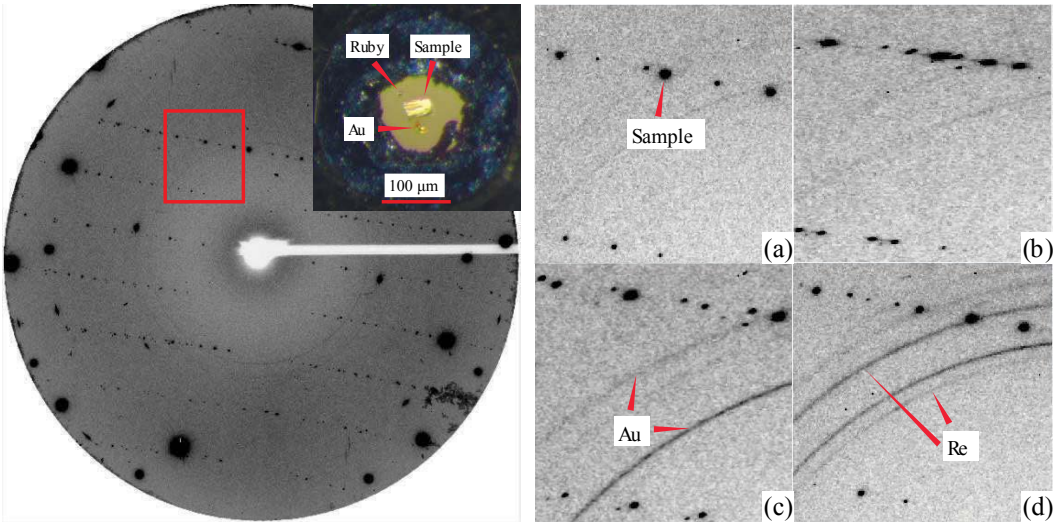

Figure 1. Left: a representative diffraction image of Ni-, Fe-bearing orthopyroxene at 11.5 GPa, and the insert figure is a representative sample photo taken at 0.7 GPa. The rectangular area shows the zoomed-in region on the Right: zoomed-in diffraction images of the rectangular area on the left, which show diffraction peaks of opx in different phases. (**a**) α-opx at 11.5 GPa; (**b**) β-opx at 12.7 GPa; (**c**) γ-opx at 16.2 GPa; (**d**) α-popx at 33.8 GPa. (Color online.)

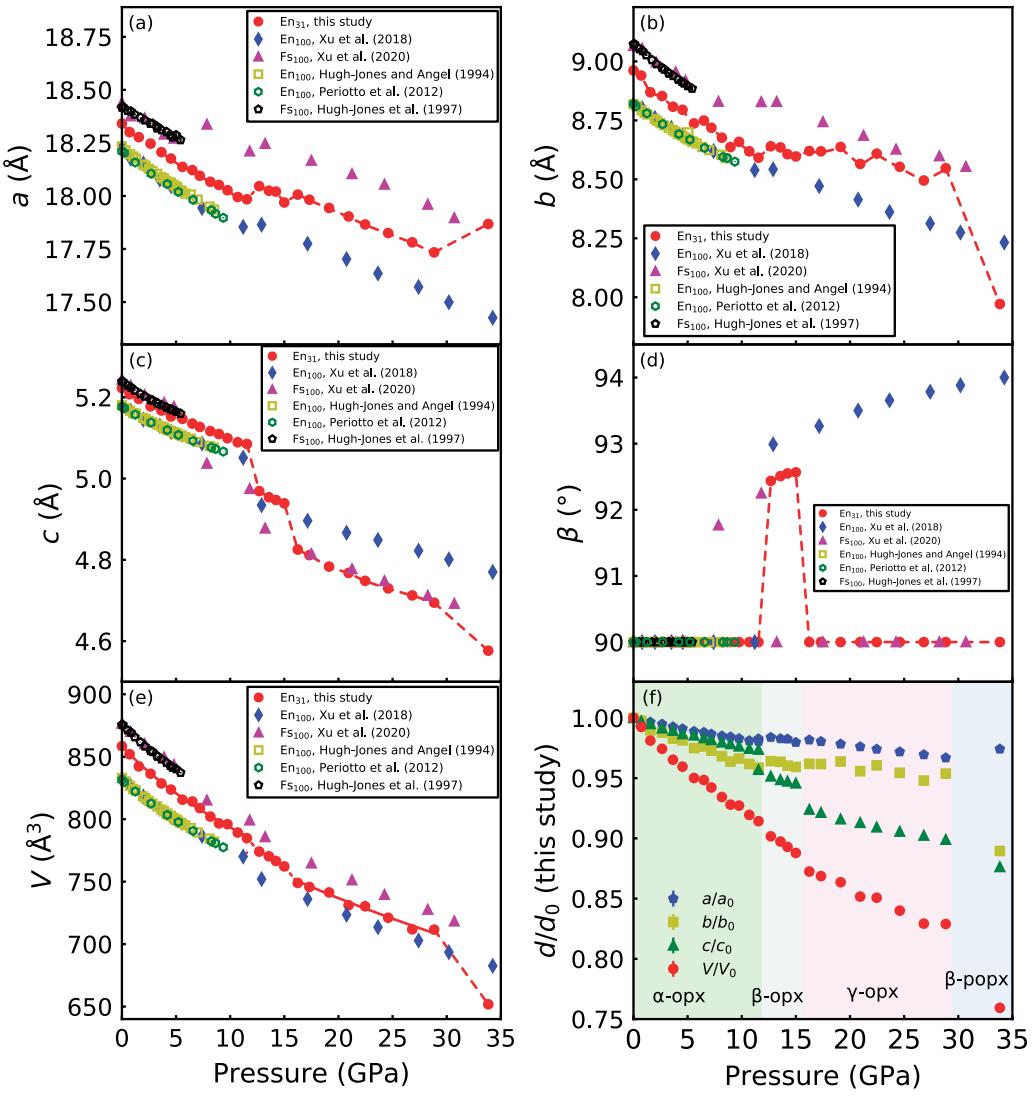

Figure 2. Unit-cell parameters and volume (**a**–**e**) of Ni-$En_{31}Fs_{65}$ as a function of pressure in comparison with En_{100} (Hugh-Jones and Angel 1994; Periotto et al. 2012; Xu et al. 2018) and Fs_{100} (Hugh-Jones et al. 1997; Xu et al. 2020); (**f**) Normalized unit-cell parameters of the Ni-$En_{31}Fs_{65}$ as a function of pressure; the shaded areas indicate the regions of the α-opx, β-opx, γ-opx, and β-popx. The red dashed lines shown in **a**–**e** are for guidance only, while the red solid lines shown in (**e**) indicate the EoS fit for α-opx and γ-opx. (Color online.)

the orthopyroxene structure from the previous study (Xu et al. 2018) as the starting model. According to the chemical formula of orthopyroxene ($M02M01T_2O_6$), the M01 and M02 sites were set to be fully occupied by Mg and Fe, while the *T* site was set to be filled with Si. We did not consider Ni in the refinement as it has a similar electron number to Fe and its insignificant content compared to Mg and Fe. We used the chemical data from the EMPA to constrain the overall contents of Fe and Mg during the structural refinement. Atoms residing at the same site were constrained to share the same atomic displacement parameters (ADPs) and the same fractional coordinates. Isotropic ADPs were used for all atoms. The crystallographic information files (CIF) are available in the Online Material[1]. The structural refinement details, atomic coordinates, occupancies, bond lengths, and polyhedral parameters are summarized in Online Materials[1] Tables S2–S7.

Results

The Ni-$En_{31}Fs_{65}$ underwent three phase transitions with increasing pressure up to 33.8 GPa. As shown by the diffraction images in Figure 1, diffraction peak changes occurred at 12.7, 16.2, and 33.8 GPa, indicating structural changes. From room pressure to 11.5 GPa, the diffraction peaks were perfectly indexed with the initial α-Opx, and the unit-cell parameters *a*, *b,* and *c* decreased with increasing pressure (Fig. 2; Online Materials[1] Table S1). At 12.7 GPa, diffraction peak indexing led to a monoclinic unit cell similar to that of the β-opx phase reported in previous studies (Dera et al. 2013a; Finkelstein et al. 2015), and analysis of the symmetry also yielded a $P2_1/c$ space group. The β-opx survived up to 15.0 GPa, and its structure was refined using the previously reported structure (Dera et al. 2013a) as the starting model (Online Materials[1] Table S3b). At 16.2 GPa, diffraction peak indexing and structural analysis yielded an orthorhombic unit cell with a *Pbca* space group (Fig. 2; Online Materials[1] Table S1), and the structure refinement indicated that this phase is the previously reported γ-opx (Online Materials[1] Table S3c; Dera

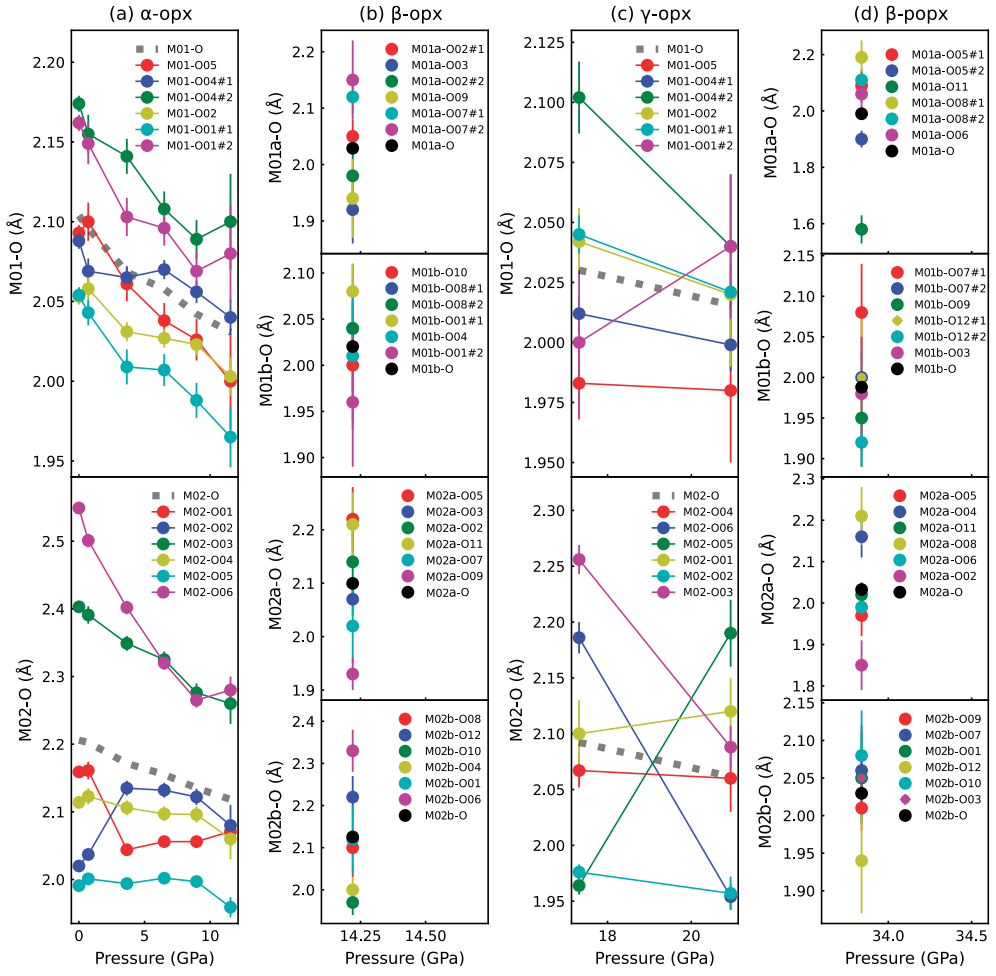

Figure 3. M-O bond lengths in the MO_6 octahedra as a function of pressure. (**a**, **b**, **c**, and **d**) The data in the region of the α-opx, β-opx, γ-opx, and β-popx, respectively. (Color online.)

et al. 2013a). The γ-opx persisted up to 28.8 GPa with its unit-cell parameters *a*, *b*, and *c* decreasing with pressure (Fig. 2). At 33.8 GPa, diffraction peak indexing also yielded an orthorhombic unit cell, but the structural analysis indicated a $P2_1ca$ space group. Its structure was solved and refined with the $P2_1ca$ space group (Online Materials[1] Table S3d), indicating that this structure is the same as the β-popx (Finkelstein et al. 2015).

The unit-cell parameters varied differently through the phase transitions. As shown in Figure 2, as α-opx transforms to β-opx, the *a* and *b* increased by 0.3 and 0.7%, respectively; by contrast, the *c* decreased by 2.3%. In the second phase transition, the *a* and *b* increased by 0.2 and 0.3%, respectively, while the *c* decreased by 2.3%. In the γ-opx → β-popx transition, the *a* increased by 0.8% while the *b* and *c* decreased by 6.7% and 2.5%, respectively. The volume drops were 1.4%, 1.7%, and 6.3% for the α-opx → β-opx, β-opx → γ-opx, and γ-opx → β-popx transitions, respectively.

The crystal structure of the α-opx has four crystallographically distinct polyhedra, $M01O_6$ and $M02O_6$ octahedra and $Si01O_4$ and $Si02O_4$ tetrahedra. $M01O_6$ and $M02O_6$ octahedra connect each other to form layers parallel to the *bc* plane. $Si01O_4$ and $Si02O_4$ tetrahedra separately form chains extending in the *c* direction. $Si01O_4$ and $Si02O_4$ chains alternately separate the layers formed by $M01O_6$ and $M02O_6$ octahedra. Within the stable region of the α-opx, the bond lengths of the $M01O_6$ octahedron decreased by 2.3–4.4% as the pressure increased from room pressure to 11.5 GPa (Fig. 3a); however, the bond lengths of the $M02O_6$ octahedron varied differently with increasing pressure; as shown in Figure 3a, the bond length of M02-O02 increased by 3.0% while the other bond lengths decreased by 1.6–11.0%. In comparison, as the pressure increased from room pressure to 11.5 GPa, the bond lengths of the $Si01O_4$ and $Si02O_4$ tetrahedra decreased by 0.2–1.2% and 0.1–3.1% (Fig. 4a), respectively. The volumes of the $M01O_6$ and $M02O_6$ octahedra decreased by 10.0 and 11.0% (Fig. 5a) over the pressure range of the α-opx, respectively, and the volumes of the $Si01O_4$ and $Si02O_4$ tetrahedra decreased by 1.0 and 3.5% (Fig. 5b), respectively.

The distortion index, quadratic elongation, and bond angle variance parameters (Robinson et al. 1971) were used to evaluate the nonideality of the coordination polyhedra. As shown in Figure 6, at room pressure, the distortion index, quadratic elongation, and bond angle variance of the $M02O_6$ octahedron are larger

than the $M01O_6$, indicating that the $M01O_6$ octahedron is closer to the ideal octahedron in comparison to the $M02O_6$ octahedron. As the pressure increased from room pressure to 11.5 GPa, the distortion index of the $M02O_6$ decreased by 41.4% (Fig. 6), but the quadratic elongation and bond angle variance only decreased by 0.9% and 0.4%, respectively. In comparison, the distortion index, quadratic elongation, and angular variance of the $M01O_6$ octahedron decreased by 1.9, 0.1, and 7.6%, respectively. The quadratic elongation of the $Si01O_4$ and $Si02O_4$ tetrahedra only decreased by 0.1% as the pressure increased to 11.5 GPa (Fig. 7); however, the distortion index of the $Si01O_4$ and $Si02O_4$ tetrahedra decreased by 23.7 and 15.7%, respectively, and the bond angle variance of these two tetrahedra decreased by 17.7 and 21.5%, respectively.

As the α-opx transformed into the β-opx, due to the symmetry change (*Pbca* → $P2_1/c$), the M01 and M02 were split into two crystallographically distinct sites (M01a/M01b and M02a/M02b). As shown in Figure 5a, at 14.2 GPa, the volumes of the $M02aO_6$ and $M02bO_6$ octahedra are larger than the volumes of the $M01aO_6$ and the $M01bO_6$ octahedra. Likewise, Si01 and Si02 were split into two Si01a/Si01b and Si02a/Si02b, respectively. The volumes of the $Si01bO_4$ and $Si02bO_4$ tetrahedra are larger than the volumes of the $Si01aO_4$ and $Si01bO_4$ tetrahedra (Fig. 5b). Nevertheless, after the β-opx transformed into the γ-opx, only four crystallographically distinct cationic sites exist in the structure, two octahedrally coordinated (M01 and M02) and two tetrahedrally coordinated (Si01 and Si02) sites. Through the α-opx → β-opx → γ-opx phase transitions, the distortion index, quadratic elongation, and bond angle variance of the $M01O_6$ octahedron did not change significantly (Fig. 6) but the quadratic elongation and bond angle variance of the $M02O_6$ octahedron decreased by 3.9 and 77.3% (Figs. 6b–6c), respectively, when pressure increased from 11.5 to 17.3 GPa.

At 33.8 GPa, as the γ-opx transformed into the β-popx, the octahedrally coordinated M01 and M02 split into M01a/M01b and M02a/M02b again, and the tetrahedrally coordinated Si01 and Si02 also split into Si01a/Si01b and Si02a/Si02b, due to the lowering of the symmetry from *Pbca* to $P2_1ca$ (Figs. 3–7). The coordination numbers of Si cations changed during this phase transition. As shown in Figure 4 and Online Materials[1] Tables S6–S7, while the Si01a remained tetrahedrally coordinated, the other three Si cations increased in coordination number (Finkelstein et al. 2015). The Si01b cation was penta-coordinated to form

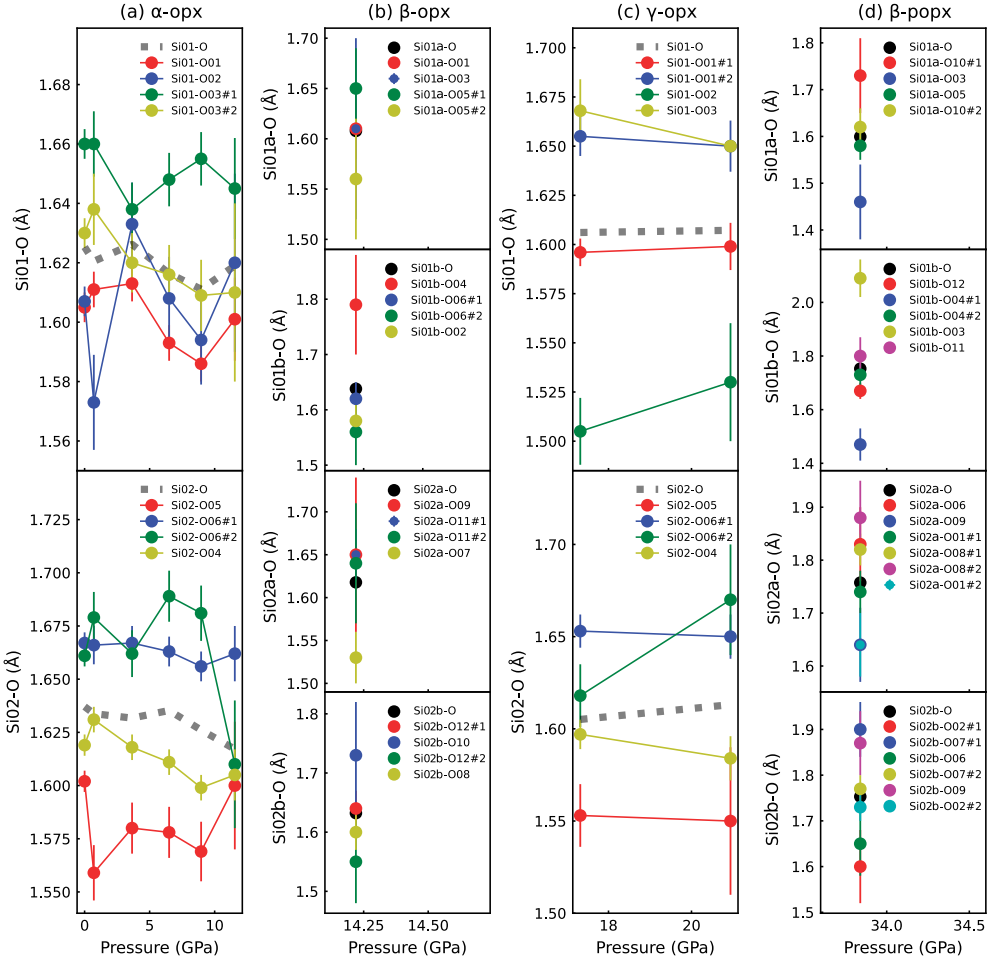

Figure 4. Si-O bond lengths as a function of pressure. (**a**, **b**, **c**, and **d**) The data in the region of the α-opx, β-opx, γ-opx, and β-popx, respectively. (Color online.)

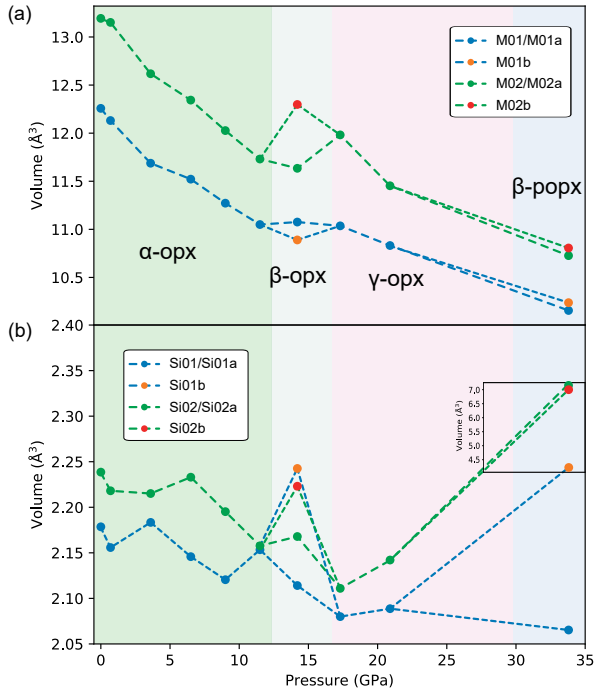

FIGURE 5. MO_6 (**a**) and $SiO_{x\ (x = 4\ or\ 5\ or\ 6)}$ (**b**) polyhedral volumes of Ni-$En_{31}Fs_{65}$ as a function of pressure. The shaded areas indicate the metastable regions of the α-opx, β-opx, γ-opx, and β-popx. (Color online.)

a highly distorted trigonal bipyramid (Fig. 7a) with a distinctly longer Si01b-O [Si01b-O03 = 2.09(7) Å; Online Materials[1] Table S7] bond than the other four [1.47(6)–1.90(7) Å]. In comparison, Si02a and Si02b were octahedrally coordinated in the β-popx (Fig. 4c), and the Si-O bond lengths in the $Si02aO_6$ and $Si02bO_6$ octahedra were 1.64(7)–1.88(7) Å and 1.60(8)–1.89(6) Å (Online Materials[1] Table S7), respectively.

The pressure-volume data of the α-opx and γ-opx were separately fitted to a Birch-Murnaghan equation of state (BMEoS) (Birch 1947) using the Eosfit7c software package (Angel et al. 2014) to obtain their EoS parameters, and we did not fit the data of β-opx and β-popx to an EoS because of their limited numbers of data points. A third-order BMEoS fit to the data of the α-opx yielded the zero-pressure volume (V_{T0}), zero-pressure bulk modulus (K_{T0}) and its pressure derivative (K'_{T0}), V_{T0} = 858.4(3) Å^3, K_{T0} = 91(5) GPa, and K'_{T0} = 8.7(17); while V_{T0} = 858.4(3) Å^3 and K_{T0} = 93(1) GPa were obtained when K'_{T0} was fixed at 8.0 [the K'_{T0} for En_{100} (Angel and Jackson 2002; Xu et al. 2018)]. We also obtained V_{T0} = 828.2(76) Å^3 and K_{T0} = 134(12) GPa for the γ-opx by fitting the pressure-volume data to the second-order BMEoS with fixed K'_{T0} = 4.

DISCUSSION

Xu et al. (2018) observed after the α-opx → β-opx phase transition the β-opx → β-opxII phase transition in a Ni-bearing Fe-free enstatite. However, this study revealed that the Ni-$En_{31}Fs_{65}$ underwent the α-opx → β-opx → γ-opx → β-popx phase transitions as the pressure increased from room pressure to 33.8 GPa, indicating that the β-opx → β-opxII phase transition does not occur for the Ni-$En_{31}Fs_{65}$. In addition, the observation of the β-opx → γ-opx phase transition in this study indicates that the phase transition of Ni-bearing Fe-rich orthopyroxene resembles Ni-free Fe-rich orthopyroxene (Fig. 8). The α-opx → β-opx → γ-opx phase transitions mainly involve the SiO_4 tetrahedral rotation as the structural change as suggested by previous studies (e.g., Dera et al. 2013a). As a result, the *c* (the extending direction of the tetrahedra chains) is decreased much more significantly in comparison to the *a* and *b* (Fig. 2) during these two phase transitions.

Previous studies reported the occurrence of the β-popx as a high-pressure phase in $En_{90}Fs_{10}$ (Finkelstein et al. 2015) and En_{100} (Serghiou et al. 2000) but not yet in more Fe-rich orthopyroxenes. $En_{90}Fs_{10}$ transforms from the α-popx to the β-popx after the α-opx → β-opx → α-popx phase transitions while En_{100} transforms into the β-popx from the β-opx (Fig. 8). Our results indicate that the β-popx also occurs in Fe-rich orthopyroxenes at high pressure, although the transition path could be different from those of $En_{90}Fs_{10}$ and En_{100} (Fig. 8). Unlike the α-opx → β-opx → γ-opx phase transitions, the γ-opx → β-popx phase transition is characterized by the coordination number increase in the Si cations. While half of the Si01 cations (Si01a) are still tetrahedrally coordinated in the β-popx as in the γ-opx, the other half (Si01b) increase from four to five in coordination number as the γ-opx transforms into β-popx. In comparison, all the Si02 (Si02a and Si02b) cations increase their coordination numbers

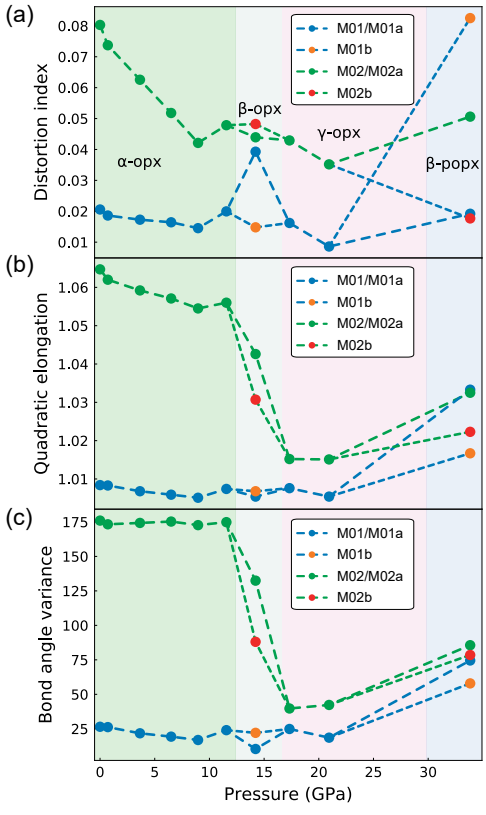

FIGURE 6. Distortion index (**a**), quadratic elongation (**b**), and bond angle variance (**c**) of the MO_6 octahedra of Ni-$En_{31}Fs_{65}$ as a function of pressure. The shaded areas indicate the stable regions of the α-opx, β-opx, γ-opx, and β-popx. (Color online.)

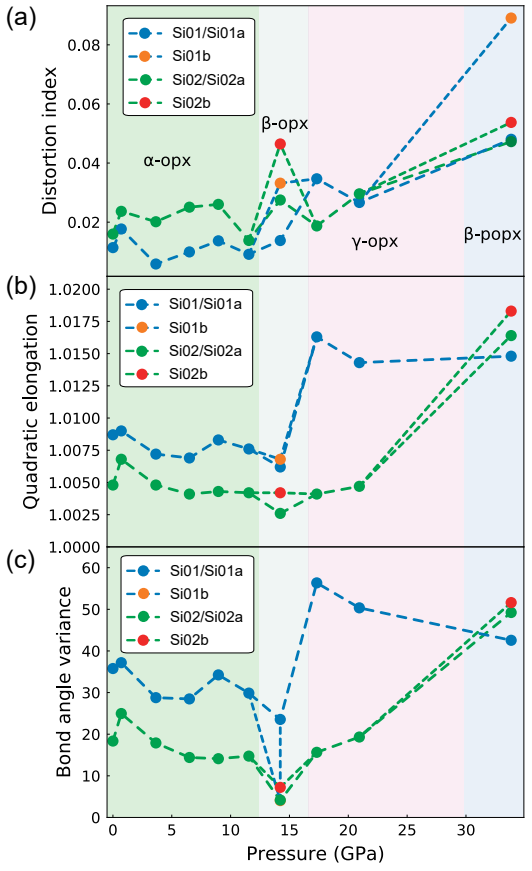

Figure 7. Distortion index (**a**), quadratic elongation (**b**), and bond angle variance (**c**) of the $SiO_{x\,(x=4\text{ or }5\text{ or }6)}$ polyhedral volume of Ni-$En_{31}Fs_{65}$ as a function of pressure. The shaded areas indicate the regions of the α-opx, β-opx, γ-opx, and β-popx. (Color online.)

from four in the γ-opx to six in the β-popx (Online Materials[1] Table S7). The increase in the coordination number of Si resulted in a much larger volume drop associated with the γ-opx → β-popx transition (6.3%) in comparison to the α-opx → β-opx (1.4%) and β-opx → γ-opx (1.7%) transitions.

The pressures of the phase transitions (P_{tr}) in the Ni-$En_{31}Fs_{65}$ follow the P_{tr}-composition relationship in the En-Fs solutions and the data do not show offset due to the presence of Ni. In addition, while the P_{tr} of the second (β-opx → γ-opx/α-popx) and third (γ-opx/α-popx/β-opx → β-popx) transitions are monotonously decreased by increasing Fe, our data confirm that there exists an offset around M_{En} = 50 for the first phase transition (α-opx → β-opx), and the Fe-effect on shifting the P_{tr} (α-opx → β-opx) is much more significant for orthopyroxenes within M_{En} <50 than that within M_{En} >50 (Fig. 8). Therefore, we refined the metastable phase boundaries of orthopyroxenes by including the Ni-$En_{31}Fs_{65}$ data in the fitting (Online Materials[1] Table S8; Fig. 8), following the track of Xu et al. (2022). For the first phase transition, since there exists an offset around M_{En} = 50, we only fit M_{En} <50 data points ($En_{44}Fs_{56}$, Ni-$En_{31}Fs_{65}$, $En_{14}Fs_{82}$, and Fs_{100}), and the result is $P_{tr} = 8.9(9) + 0.09(3)M_{En}$, $R^2 = 0.86$; for the second phase transition, a linear fitting of 7 data points ($En_{90}Fs_{10}$, $En_{70}Fs_{30}$, $En_{55}Fs_{45}$, $En_{44}Fs_{56}$, Ni-$En_{31}Fs_{65}$, $En_{14}Fs_{82}$, and Fs_{100}) yielded $P_{tr} = 11.4(9) + 0.18(2)M_{En}$, $R^2 = 0.95$; for the third phase transition, 3 data points (Ni-$En_{31}Fs_{65}$, En_{90}, and En_{100}) were used for a linear fitting, and the resulted formula is $P_{tr} = 28.0(12) + 0.11(1)M_{En}$, $R^2 = 0.98$.

Implications

In cold subducting slabs, the temperature in the slab could be several hundred K lower than that of the normal mantle (Syracuse et al. 2010; King et al. 2015). Under such low-temperature conditions, pyroxene could survive as metastable phases in the cold subducting slab to the transition zone since the pyroxene → majorite transition is largely inhibited in geological timescales under the low-temperature conditions in the slab (Nishi et al. 2013; van Mierlo et al. 2013). It has been proposed that metastable pyroxene transforms into akimotoite (Hogrefe et al. 1994) in the transition zone, which plays an important role in subducting slab dynamics. However, in situ, high-pressure XRD experiments (Pakhomova et al. 2017; Lazarz et al. 2019) suggest that metastable pyroxene likely does not transform into akimotoite directly. On the contrary, high-pressure SCXRD experiments have revealed the pyroxene → post-pyroxene (like the γ-opx → β-popx phase transition in this study) transition in several pyroxene minerals. The post-pyroxene means that the structure remains pyroxene-like M01 and M02 sites, but fivefold- and sixfold-coordination exists in its Si cations (Finkelstein et al. 2015).

Natural pyroxene minerals are divided in terms of their crystal structures (orthorhombic and monoclinic) into orthopyroxene and clinopyroxene (Nesse 2000). For the subducting slab, the most important end-members of orthopyroxene are En_{100} and Fs_{100}. Diopside (Di, $CaMgSi_2O_6$) and hedenbergite (Hd, $CaFeSi_2O_6$) are the most important end-member Ca-clinopyroxenes; jadeite

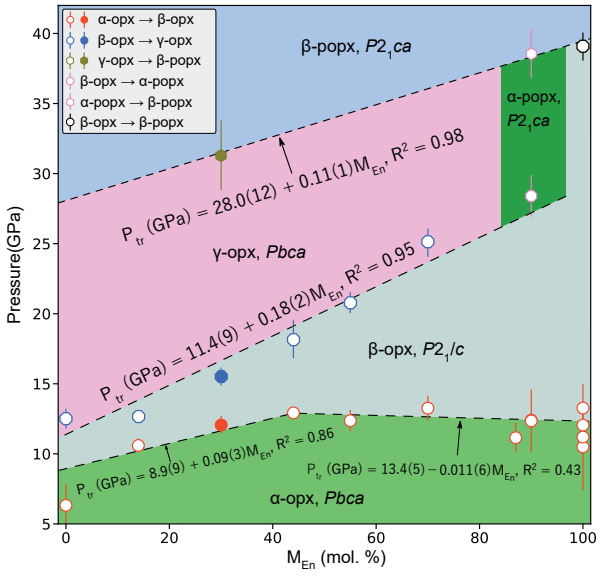

Figure 8. Pressure-induced phase transitions of orthopyroxene as a function of M_{En} (molar percentage of enstatite from Fig. 2 in Xu et al. 2022). The dashed lines represent weighted regressions of the data (P-M_{En}, Online Materials[1] Table S8) for the phase transitions and the regression equation of each dashed line is shown nearby. Note that $P_{tr} = 13.4(5) - 0.011(6)M_{En}$, $R^2 = 0.43$ is the formula adopted from Xu et al. (2022). The solid symbols represent the data of Ni-$En_{31}Fs_{65}$ obtained in this study. (Color online.)

(Jd, $NaAlSi_2O_6$) and aegirine (Aeg, $NaFe^{3+}Si_2O_6$) are the most important end-member Na-clinopyroxenes. The common Ca- and Na-free end-member clinopyroxenes are clinoenstatite (Cen, $MgSiO_3$) and clinoferrosilite (Cfs, $FeSiO_3$).

The pyroxene → post-pyroxene transition has been revealed at room temperature and high pressure in both orthopyroxene and clinopyroxene (Fig. 9). The post-pyroxene structure of orthopyroxene has been obtained in En_{100} (Serghiou et al. 2000), En_{90} (Finkelstein et al. 2015), and Ni-$En_{31}Fs_{65}$ (This study) at 39.0, 38.6, and 31.3 GPa, respectively. In comparison, the pyroxene → post-pyroxene transition occurs at 43.2 GPa in clinoenstatite (Lazarz et al. 2019) and 33.0 GPa in clinoferrosilite (Pakhomova et al. 2017). The Ca-clinopyroxenes transform from the initial pyroxene structure into their post-pyroxene structure at distinctly higher pressures than orthopyroxenes. As shown in Figure 9, the post-pyroxene structure occurs in Di_{75} (Hu et al. 2017) and Di_{97} (Plonka et al. 2012) at 51.8 and 49.4 GPa, respectively. Synchrotron-based nuclear forward scattering experiment observed a phase transition in Hd_{100} between 53 and 68 GPa (Zhang et al. 1999) which might be related to the pyroxene → post-pyroxene transition. On the contrary, the pyroxene → post-pyroxene transition has not yet been reported in Na-clinopyroxene. SCXRD up to 30.4 GPa did not observe any phase transition in Jd_{100} (Posner et al. 2014); likewise, no phase transition occurs in a solid solution $Di_{51}Jd_{49}$ up to 47 GPa (Zhang et al. 2016). The pyroxene → post-pyroxene transition was also not obtained in Aeg_{100} up to 60 GPa (Xu et al. 2017b). Since the pyroxene → post-pyroxene transition seems to occur at lower pressures in Fe-rich pyroxenes than in Fe-poor pyroxenes (Fig. 9), this phase transition might occur in Na-clinopyroxenes at pressures higher than 60 GPa.

Therefore, the pyroxene → post-pyroxene transition seems unlikely to occur in the Earth's transition zone (440–660 km) based on the results of in situ room-temperature high-pressure experiments. As shown in Figure 9, the pyroxene → post-pyroxene transition occurs in Ni-$En_{31}Fs_{65}$ at 31.3 GPa (corresponding to a depth of ~850 km), which has been the lowest pressure thus far that enables this phase transition. Increasing temperature likely enables this phase transition to occur at lower pressures than at room temperature (Hu et al. 2017). However, single-crystal XRD studies on pyroxene minerals at simultaneously high pressure and high temperature up to the pressures corresponding to the transition zone depths are still limited. High-pressure-temperature single-crystal XRD up to ~25 GPa and 800 K did not observe the pyroxene → post-pyroxene transition in orthopyroxenes with various compositions (e.g., Xu et al. 2020). The post-pyroxene was also not observed in natural augite (Di_{74}; Xu et al. 2017a) and in a natural omphacite ($Di_{57}Jd_{43}$; Xu et al. 2019) at high pressure-temperature up to ~25 GPa and 700 K. Geophysical modeling estimated the current temperatures in cold stagnant slab interior in the transition zone to range from ~800 to ~1200 K depending on the location of the slab (King et al. 2015). Therefore, more high-pressure-temperature investigations at temperatures up to 1200 K are needed on the pyroxene → post-pyroxene transition in different kinds of pyroxene for a better understanding of its role in the subducting slab dynamics.

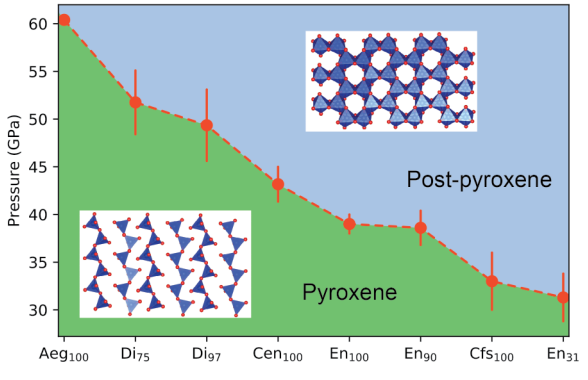

Figure 9. Phase transition pressure of the pyroxene → post-pyroxene for orthopyroxene (En = enstatite) and clinopyroxene (Aeg = aegirine; Di = diopside; Cen = clinoenstatite; Cfs = clinoferrosilite). The insert figure at the bottom left shows a layer of typical chains formed by SiO_4 tetrahedra in orthopyroxene while that at the top right shows a layer of SiO_6 octahedra in post-pyroxene. (Color online.)

Acknowledgments

We acknowledge Sergey N. Tkachev for the gas loading assistance. We thank two anonymous reviewers for their helpful comments, which helped to improve the quality of this manuscript. We thank O. Tschauner for handling this manuscript.

Funding

This work was supported by the "Hundred Talents Program of the Chinese Academy of Sciences," the National Natural Science Foundation of China (42172048), and Guizhou Provincial Outstanding Youth Science and Technology Talent Project. The diffraction experiments were performed at GeoSoilEnviroCARS, Sector13-BM-C, Partnership for Extreme Crystallography program (PX^2), Advanced Photon Source (APS), and Argonne National Laboratory. GeoSoilEnviroCARS is supported by the National Science Foundation–Earth Sciences (EAR-1634415) and the Department of Energy–Geosciences (DE-FG02-94ER14466). PX^2 program is supported by COMPRES under NSF Cooperative Agreement EAR-1661511. The use of the COMPRES-GSECARS gas loading system was supported by COMPRES under NSF Cooperative Agreement EAR-1661511 and by GSECARS. Use of the APS was supported by the U.S. Department of Energy, Office of Science, Office of Basic Energy Sciences, under Contract No. DE-AC02-06CH11357.

References cited

Angel, R.J. and Jackson, J.M. (2002) Elasticity and equation of state of orthoenstatite, $MgSiO_3$. American Mineralogist, 87, 558–561, https://doi.org/10.2138/am-2002-0419.

Angel, R.J., Alvaro, M., and Gonzalez-Platas, J. (2014) EosFit7c and a Fortran module (library) for equation of state calculations. Zeitschrift für Kristallographie. Crystalline Materials, 229, 405–419, https://doi.org/10.1515/zkri-2013-1711.

Birch, F. (1947) Finite elastic strain of cubic crystals. Physical Review, 71, 809–824, https://doi.org/10.1103/PhysRev.71.809.

Bodinier, J.L. and Godard, M. (2007) Orogenic, ophiolitic, and abyssal peridotites. In H.D. Holland and K.K. Turekian, Eds., Treatise on Geochemistry, 2, 1–73. Pergamon.

Dera, P., Finkelstein, G.J., Duffy, T.S., Downs, R.T., Meng, Y., Prakapenka, V., and Tkachev, S. (2013a) Metastable high-pressure transformations of orthoferrosilite Fs_{82}. Physics of the Earth and Planetary Interiors, 221, 15–21, https://doi.org/10.1016/j.pepi.2013.06.006.

Dera, P., Zhuravlev, K., Prakapenka, V., Rivers, M.L., Finkelstein, G.J., Grubor-Urosevic, O., Tschauner, O., Clark, S.M., and Downs, R.T. (2013b) High pressure single-crystal micro X-ray diffraction analysis with GSE_ADA/RSV software. High Pressure Research, 33, 466–484, https://doi.org/10.1080/08957959.2013.806504.

Dolomanov, O.V., Bourhis, L.J., Gildea, R.J., Howard, J.A., and Puschmann, H. (2009) OLEX2: A complete structure solution, refinement and analysis program. Journal of Applied Crystallography, 42, 339–341, https://doi.org/10.1107/S0021889808042726.

Fei, Y., Ricolleau, A., Frank, M., Mibe, K., Shen, G., and Prakapenka, V. (2007) Toward an internally consistent pressure scale. Proceedings of the National Academy of Sciences of the United States of America, 104, 9182–9186, https://doi.org/10.1073/pnas.0609013104.

Finkelstein, G.J., Dera, P.K., and Duffy, T.S. (2015) Phase transitions in orthopyroxene (En_{90}) to 49 GPa from single-crystal X-ray diffraction. Physics of the Earth and Planetary Interiors, 244, 78–86, https://doi.org/10.1016/j.pepi.2014.10.009.

Hogrefe, A., Rubie, D., Sharp, T., and Seifert, F. (1994) Metastability of enstatite in deep subducting lithosphere. Nature, 372, 351–353, https://doi.org/10.1038/372351a0.

Hu, Y., Kiefer, B., Bina, C.R., Zhang, D., and Dera, P.K. (2017) High-pressure γ-$CaMgSi_2O_6$: Does penta-coordinated silicon exist in the Earth's mantle? Geophysical Research Letters, 44, 11,340–11,348, https://doi.org/10.1002/2017GL075424.

Hugh-Jones, D.A. and Angel, R.J. (1994) A compressional study of $MgSiO_3$ orthoenstatite up to 8.5 GPa. American Mineralogist, 79, 405–410.

Hugh-Jones, D., Chopelas, A., and Augel, R. (1997) Tetrahedral compression in $(Mg,Fe)SiO_3$ orthopyroxenes. Physics and Chemistry of Minerals, 24, 301–310, https://doi.org/10.1007/s002690050042.

Ishimaru, S. and Arai, S. (2008) Nickel enrichment in mantle olivine beneath a volcanic front. Contributions to Mineralogy and Petrology, 156, 119–131, https://doi.org/10.1007/s00410-007-0277-6.

King, S.D., Frost, D.J., and Rubie, D.C. (2015) Why cold slabs stagnate in the transition zone. Geology, 43, 231–234, https://doi.org/10.1130/G36320.1.

Lazarz, J.D., Dera, P., Hu, Y., Meng, Y., Bina, C.R., and Jacobsen, S.D. (2019) High-pressure phase transitions of clinoenstatite. American Mineralogist, 104, 897–904, https://doi.org/10.2138/am-2019-6740.

Li, L., Sun, N., Shi, W., Mao, Z., Yu, Y., Zhang, Y., and Lin, J.F. (2022) Elastic anomalies across the α-β phase transition in orthopyroxene: Implication for the metastable wedge in the cold subduction slab. Geophysical Research Letters, 49, e2022GL099366, https://doi.org/10.1029/2022GL099366.

Lin, C.-M., Chao, J., and Lin, C.-C. (2005) Metastable phase transition of orthoenstatite ($MgSiO_3$) under high pressure. Solid State Sciences, 7, 293–297, https://doi.org/10.1016/j.solidstatesciences.2004.10.005.

Momma, K. and Izumi, F. (2011) VESTA 3 for three-dimensional visualization of crystal, volumetric and morphology data. Journal of Applied Crystallography, 44, 1272–1276, https://doi.org/10.1107/S0021889811038970.

Nesse, W.D. (2000) Introduction to Mineralogy, 442 p. Oxford University Press.

Nishi, M., Kubo, T., Ohfuji, H., Kato, T., Nishihara, Y., and Irifune, T. (2013) Slow Si-Al interdiffusion in garnet and stagnation of subducting slabs. Earth and Planetary Science Letters, 361, 44–49, https://doi.org/10.1016/j.epsl.2012.11.022.

Pakhomova, A., Ismailova, L., Bykova, E., Bykov, M., Boffa Ballaran, T., and Dubrovinsky, L. (2017) A new high-pressure phase transition in clinoferrosilite: In situ single-crystal X-ray diffraction study. American Mineralogist, 102, 666–673, https://doi.org/10.2138/am-2017-5853.

Periotto, B., Balić-Žunić, T., Nestola, F., Katerinopoulou, A., and Angel, R.J. (2012) Re-investigation of the crystal structure of enstatite under high-pressure conditions. American Mineralogist, 97, 1741–1748, https://doi.org/10.2138/am.2012.4157.

Plonka, A.M., Dera, P., Irmen, P., Rivers, M.L., Ehm, L., and Parise, J.B. (2012) β-diopside, a new ultrahigh-pressure polymorph of $CaMgSi_2O_6$with six-coordinated silicon. Geophysical Research Letters, 39, 2012GL054023, https://doi.org/10.1029/2012GL054023.

Posner, E.S., Dera, P., Downs, R.T., Lazarz, J.D., and Irmen, P. (2014) High-pressure single-crystal X-ray diffraction study of jadeite and kosmochlor. Physics and Chemistry of Minerals, 41, 695–707, https://doi.org/10.1007/s00269-014-0684-y.

Ringwood, A.E. (1982) Phase transformations and differentiation in subducted lithosphere: Implications for mantle dynamics, basalt petrogenesis, and crustal evolution. The Journal of Geology, 90, 611–643, https://doi.org/10.1086/628721.

Rivers, M., Prakapenka, V.B., Kubo, A., Pullins, C., Holl, C.M., and Jacobsen, S.D. (2008) The COMPRES/GSECARS gas-loading system for diamond anvil cells at the Advanced Photon Source. High Pressure Research, 28, 273–292, https://doi.org/10.1080/08957950802333593.

Robinson, K., Gibbs, G.V., and Ribbe, P.H. (1971) Quadratic elongation: A quantitative measure of distortion in coordination polyhedra. Science, 172, 567–570, https://doi.org/10.1126/science.172.3983.567.

Serghiou, G., Boehler, R., and Chopelas, A. (2000) Reversible coordination changes in crystalline silicates at high pressure and ambient temperature. Journal of Physics Condensed Matter, 12, 849–857, https://doi.org/10.1088/0953-8984/12/6/309.

Sheldrick, G.M. (2008) A short history of SHELX. Acta Crystallographica Section A: Foundations of Crystallography, 64, 112–122, https://doi.org/10.1107/S0108767307043930.

Syracuse, E.M., van Keken, P.E., and Abers, G.A. (2010) The global range of subduction zone thermal models. Physics of the Earth and Planetary Interiors, 183, 73–90, https://doi.org/10.1016/j.pepi.2010.02.004.

van Mierlo, W., Langenhorst, F., Frost, D., and Rubie, D. (2013) Stagnation of subducting slabs in the transition zone due to slow diffusion in majoritic garnet. Nature Geoscience, 6, 400–403, https://doi.org/10.1038/ngeo1772.

Xu, J., Zhang, D., Dera, P., Zhang, B., and Fan, D. (2017a) Experimental evidence for the survival of augite to transition zone depths, and implications for subduction zone dynamics. American Mineralogist, 102, 1516–1524, https://doi.org/10.2138/am-2017-5959.

Xu, J., Zhang, D., Fan, D., Downs, R.T., Hu, Y., and Dera, P. (2017b) Isosymmetric pressure-induced bonding increase changes compression behavior of clinopyroxenes across jadeite-aegirine solid solution in subduction zones. Journal of Geophysical Research. Solid Earth, 122, 142–157, https://doi.org/10.1002/2016JB013502.

Xu, J., Zhang, D., Fan, D., Zhang, J.S., Hu, Y., Guo, X., Dera, P., and Zhou, W. (2018) Phase transitions in orthoenstatite and subduction zone dynamics: Effects of water and transition metal ions. Journal of Geophysical Research. Solid Earth, 123, 2723–2737, https://doi.org/10.1002/2017JB015169.

Xu, J., Zhang, D., Fan, D., Dera, P.K., Shi, F., and Zhou, W. (2019) Thermoelastic properties of eclogitic garnets and omphacites: Implications for deep subduction of oceanic crust and density anomalies in the upper mantle. Geophysical Research Letters, 46, 179–188, https://doi.org/10.1029/2018GL081170.

Xu, J., Fan, D., Zhang, D., Guo, X., Zhou, W., and Dera, P.K. (2020) Phase transition of enstatite-ferrosilite solid solutions at high pressure and high temperature: Constraints on metastable orthopyroxene in cold subduction. Geophysical Research Letters, 47, e2020GL087363.

Xu, J., Fan, D., Zhang, D., Ma, M., Zhou, Y., Tkachev, S.N., Zhou, W., and Dera, P.K. (2022) Phase transitions of Fe-, Al- and Ca-bearing orthopyroxenes at high pressure and high temperature: Implications for metastable orthopyroxenes in stagnant slabs. Journal of Geophysical Research: Solid Earth, 127, e2021JB023133.

Zhang, L., Stanek, J., Hafner, S., Ahsbahs, H., Grünsteudel, H., and Metge, J. (1999) ^{57}Fe nuclear forward scattering of synchrotron radiation in hedenbergite $CaFeSi_2O_6$ at hydrostatic pressures up to 68 GPa. American Mineralogist, 84, 447–453, https://doi.org/10.2138/am-1999-0329.

Zhang, J.S., Dera, P., and Bass, J.D. (2012) A new high-pressure phase transition in natural Fe-bearing orthoenstatite. American Mineralogist, 97, 1070–1074, https://doi.org/10.2138/am.2012.4072.

Zhang, D., Jackson, J.M., Chen, B., Sturhahn, W., Zhao, J., Yan, J., and Caracas, R. (2013a) Elasticity and lattice dynamics of enstatite at high pressure. Journal of Geophysical Research. Solid Earth, 118, 4071–4082, https://doi.org/10.1002/jgrb.50303.

Zhang, J.S., Reynard, B., Montagnac, G., Wang, R.C., and Bass, J.D. (2013b) Pressure-induced *Pbca-P*$2_1/c$ phase transition of natural orthoenstatite: Compositional effect and its geophysical implications. American Mineralogist, 98, 986–992, https://doi.org/10.2138/am.2013.4345.

Zhang, J.S., Reynard, B., Montagnac, G., and Bass, J.D. (2014) Pressure-induced *Pbca–P*$2_1/c$ phase transition of natural orthoenstatite: The effect of high temperature and its geophysical implications. Physics of the Earth and Planetary Interiors, 228, 150–159, https://doi.org/10.1016/j.pepi.2013.09.008.

Zhang, D., Hu, Y., and Dera, P.K. (2016) Compressional behavior of omphacite to 47 GPa. Physics and Chemistry of Minerals, 43, 707–715, https://doi.org/10.1007/s00269-016-0827-4.

Zhang, D., Dera, P.K., Eng, P.J., Stubbs, J.E., Zhang, J.S., Prakapenka, V.B., and Rivers, M.L. (2017) High Pressure Single Crystal Diffraction at PX^2. Journal of Visualized Experiments, 119, e54660.

Manuscript received November 21, 2022
Manuscript accepted May 31, 2023
Accepted manuscript online June 7, 2023
Manuscript handled by Oliver Tschauner

Endnote:

[1]Deposit item AM-24-48879. Online Materials are free to all readers. Go online, via the table of contents or article view, and find the tab or link for supplemental materials. The CIF has been peer-reviewed by our Technical Editors.